ADVANCED
QUANTUM
TECHNOLOGIES
www.advquantumtech.com

Integrated and Portable Magnetometer Based on Nitrogen-Vacancy Ensembles in Diamond

Felix M. Stürner, Andreas Brenneis, Thomas Buck, Julian Kassel, Robert Rölver, Tino Fuchs, Anton Savitsky, Dieter Suter, Jens Grimmel, Stefan Hengesbach, Michael Förtsch, Kazuo Nakamura, Hitoshi Sumiya, Shinobu Onoda, Junichi Isoya, and Fedor Jelezko*

Magnetic field sensors that exploit quantum effects have shown that they can outperform classical sensors in terms of sensitivity enabling a range of novel applications in future, such as a brain machine interface. Negatively charged nitrogen-vacancy (NV) centers in diamond have emerged as a promising high sensitivity platform for measuring magnetic fields at room temperature. Transferring this technology from laboratory setups into products and applications, the total size of the sensor, the overall power consumption, and the costs need to be reduced and optimized. Here, a fiber-based NV magnetometer featuring a complete integration of all functional components is demonstrated without using any bulky laboratory equipment. This integrated prototype allows portable measurement of magnetic fields with a sensitivity of 344 pT Hz$^{-1/2}$.

1. Introduction

Sensing and metrology by means of adapting quantum technologies have attracted a high degree of attention in recent years, as evidenced by numerous large publicly funded programs worldwide and a growing interest of companies in this field of technology. A very promising quantum sensing approach, which represents the transition from basic research to product application, is based on the negatively charged nitrogen-vacancy (NV) centers in diamond. These color centers comprise high magnetic sensitivity at ambient conditions with large dynamic range and high spatial resolution.[1,2] In addition, this technology can be applied to measure temperature,[3] electric fields,[4] and pressure.[5]

Hall sensors, magnetoresistance sensors, optically pumped magnetometers (OPMs), and superconducting interference devices (SQUIDs) are state-of-the-art magnetometers. Especially, Hall and tunnel magnetoresistance sensors are widely spread in consumer electronic devices, e.g., smartphones, with a detection limit typically 1 nT Hz$^{-1/2}$. SQUIDs show exceptional magnetic field detection performance with sensitivities in the fT Hz$^{-1/2}$ regime, require though a bulky and costly infrastructure including

---

F. M. Stürner, Dr. A. Brenneis, T. Buck, J. Kassel, Dr. R. Rölver, Dr. T. Fuchs
Corporate Sector Research and Advance Engineering
Robert Bosch GmbH
Robert-Bosch-Campus 1, Renningen 71272, Germany
E-mail: Andreas.Brenneis@de.bosch.com

F. M. Stürner, Prof. F. Jelezko
Institute for Quantum Optics and Center for Integrated Quantum Science and Technology (IQST)
Ulm University
Albert-Einstein-Allee 11, Ulm 89081, Germany

Dr. A. Savitsky, Prof. D. Suter
Fakultät Physik
Technische Universität Dortmund
Otto-Hahn-Straße 4a, Dortmund 44227, Germany

Dr. J. Grimmel, Dr. S. Hengesbach, Dr. M. Förtsch
Q.ANT GmbH
Handwerkstraße 29, Stuttgart 70565, Germany

K. Nakamura
Leading-Edge Energy System Research Institute, Fundamental Technology Dept.
Tokyo Gas Co., Ltd.
Yokohama 230-0045, Japan

Dr. H. Sumiya
Advanced Materials Laboratory
Sumitomo Electric Industries, Ltd.
Itami 664-0016, Japan

Dr. S. Onoda
Takasaki Advanced Radiation Research Institute
National Institutes for Quantum and Radiological Science and Technology
Takasaki 370-1292, Japan

Prof. J. Isoya
Faculty of Pure and Applied Sciences
University of Tsukuba
Tsukuba 305-8573, Japan

DOI: 10.1002/qute.202000111

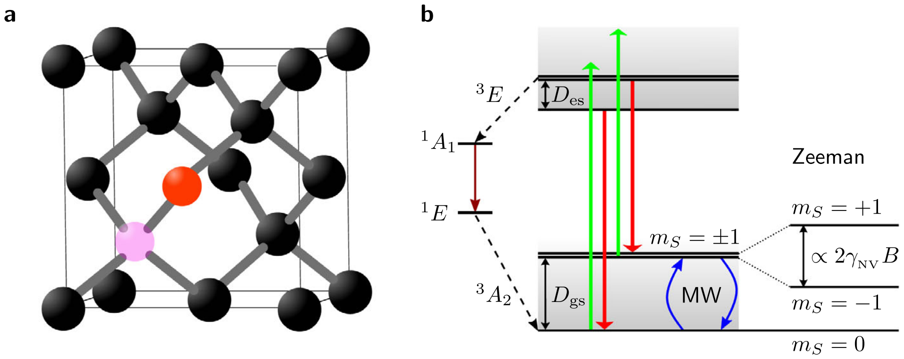

Figure 1. NV center in diamond and its energy diagram. a) The negatively charged nitrogen-vacancy center is a color center in the lattice of the diamond consisting of a nitrogen atom (red) and an adjacent vacancy (light purple). Carbon atoms are shown as black spheres. The NV center can be orientated along four possible crystallographic axes of the diamond. b) Schematic of the energy level scheme of the negatively charged NV center. Both the ground state ($^3A_2$) and the excited state (^3E) are spin triplets. The zero-field splitting energy of the ground state is $D_{\mathrm{gs}} \approx 2.87$ GHz. The electron spin states of the $S = 1$ system are denoted with the spin quantum numbers $m_s = 0$ and $m_s = \pm 1$. Spin population can be optically pumped into the ^3E states by green light (green arrows), from which the spins decay back to $^3A_2$ under the emission of red fluorescence (red arrows), while the spin quantum number is conserved. Spins in the $m_s = \pm 1$ have a higher probability than those with $m_s = 0$ to undergo intersystem crossing via the states $^1A_1$ and ^1E with infrared emission (dark red arrow). This results in a reduced fluorescence emission and a polarization into the $m_s = 0$ ground state. A resonant microwave field enables population transfer between $m_s = 0$ and $m_s = \pm 1$ states. The $m_s = \pm 1$ states split under the application of an external magnetic field, which can be optically detected in an ODMR measurement.

cryogenic cooling.[6] By contrast, NV diamond and OPMs can be operated at room temperature and have the potential to be miniaturized. While the latter suffers from a limited dynamic range, NV diamond sensors can be operated at large background fields, e.g., Earth's magnetic field.

The magnetic field detection of the NV centers relies on the magnetic interaction of the electron spin via the Zeeman effect. The NV spin state can be optically initialized, manipulated using microwave fields, and optically read out with long coherence times.[7] Limitations on the achievable sensor performance for NV ensembles arise from several factors, which are interconnected and mutually dependent, and impede a straightforward optimization of the performance. The sensitivity depends on the quality of the diamond material with parameters of NV concentration, NV orientation, NV charge state, isotopic compositions, concentration of paramagnetic impurities, and the material parameters, such as strain limiting the coherence properties of the spins.[8] For the optical initialization of the NV spins, the optical power, wavelength, polarization, and homogeneity of the excitation light need to be optimized for a high sensitivity NV ensemble magnetometer.[9] Further effort is necessary to provide a homogeneous offset magnetic field in addition to a sufficiently strong and homogeneous microwave field.[10] Due to diamond's high refractive index, solutions need to be developed to efficiently extract the fluorescence light that is emitted by the NV centers.[11] Furthermore, the implementation of pulsed measurement protocols can improve the sensitivity by decreasing the impact of noise sources, e.g., decoherence due to paramagnetic spins or temperature fluctuations.[12,13]

Recent achievements in NV diamond magnetometry have shown detection of AC fields with a sensitivity of 0.9 pT Hz$^{-1/2}$,[2] recording of neuronal action potentials with a sensitivity of 15 pT Hz$^{-1/2}$,[12] and a sensitivity of 0.9 pT Hz$^{-1/2}$ in the low frequency range.[14] Vector magnetometry experiments have been demonstrated for DC[15] and AC fields[16] enabling NV centers for a wide range of applications. Potential applications could be implemented in the field of medical diagnostics or brain–machine interface.[17] In addition to high sensitivity, NV center magnetometers can cover a high dynamic range. However, most of these impressive results have been achieved on bulky setups with constraints to a laboratory environment. For a mobile application of an NV-based magnetometer it is indispensable to integrate and miniaturize the sensor components to a compact and portable device. Based on different approaches, recent works have focused on the development of prototypes that can enable the NV centers for industrial product applications.[18–23]

Here, we demonstrate a fiber-integrated magnetometer based on NV centers in diamond. The compact design of the magnetic field sensor was achieved by using a single-mode fiber for the optical initialization of the NV centers and deploying a balanced detection scheme built up by two photodiodes positioned close to the diamond. Furthermore, our integrated prototype comprises all necessary components, such as offset magnetic field, laser source, microwave generator, and signal processing unit. This portable setup yields a sensitivity of ≈ 344 pT Hz$^{-1/2}$.

2. Materials and Methods

The NV center is a color center in the lattice structure of a diamond consisting of a nitrogen atom and an adjacent vacancy spot, see **Figure 1**. In its negatively charged state, the NV center is a spin $S = 1$ system with spin triplets both in the ground state ($^3A_2$) and the excited state (^3E), see Figure 1b. These spin states are denoted with the spin quantum numbers $m_s = 0$ and $m_s = \pm 1$. Optical pumping transfers spin population from the ground to the excited states, while the spin quantum number is maintained. However, the efficiency of the nonradiative relaxation path to the ground state via the singlet states strongly depends on the spin quantum number resulting in a spin dependent fluorescence intensity and optical pumping. The NV

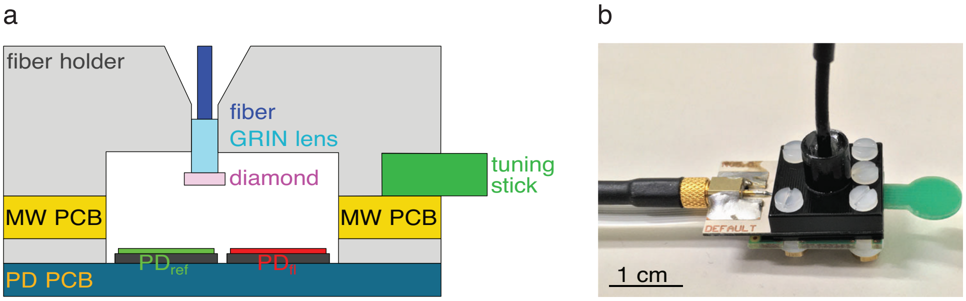

Figure 2. Assembly of the sensor head. a) Schematic cross-section of the sensor head including the used components (optical fiber, GRIN rod lens, 3D-printed fiber holding construction, diamond, microwave board (MW PCB), resonator tuning stick, MMCX connector, and the balanced photodetection board (PD PCB) including two photodiodes with different coating, PD$_{\mathrm{ref}}$ and PD$_{\mathrm{fl}}$, and electronic components at the back of this PCB. b) Photoimage of the NV sensor.

centers are susceptible to magnetic fields through the Zeeman effect yielding a magnetic field dependent electron spin resonance for the spin transitions from the $m_s = 0$ to the $m_s = \pm 1$ ground states, see Figure 1b. Zeeman splitting leads to a shift of the resonance frequencies $f_\pm$ of the spin transitions of NV centers as[23]

$$f_\pm \approx D_{\mathrm{gs}} \pm \gamma_{\mathrm{NV}} B_0 \tag{1}$$

where $D_{\mathrm{gs}} \approx 2.87$ GHz is the zero-field splitting due to the spin–spin interaction at room temperature, $\gamma_{\mathrm{NV}} = \mu_{\mathrm{B}} g_{\mathrm{s}}/h \approx 28.024\ \mathrm{GHz\,T^{-1}}$ the gyromagnetic ratio with μ_{B} the Bohr magneton, $g_{\mathrm{s}} \approx 2.0028$ the approximately isotropic g-factor, h the Planck constant, and B_0 the projection of the magnetic field on the corresponding NV axis.[24] Due to the Zeeman effect, the shift of the resonance frequencies from D_{gs} is proportional to the magnetic field.

The optically detected magnetic resonance (ODMR), as a standard technique, can be performed either in a continuous wave (CW) or pulsed mode.[25] The CW ODMR measurement is characterized by a simultaneous application of excitation light and microwave field to initialize and manipulate the NV spins. It is typically easier to implement compared to the pulsed scheme.

One important figure of merit for magnetometers is the magnetic sensitivity characterizing the minimal magnetic field δB_{min}, which can be detected by the sensor within a given measurement time t. Due to the optical readout of the NV spin states, the sensitivity η_{PSN} is limited by photon shot-noise and is given by[11]

$$\eta_{\mathrm{PSN}} = \delta B_{\mathrm{min}} \cdot \sqrt{t} \approx P_F \cdot \frac{1}{\gamma_{\mathrm{NV}}} \cdot \frac{\Delta \nu}{C} \cdot \frac{1}{\sqrt{R}} \tag{2}$$

where P_{F} is a numerical factor resulting from the shape of the resonance with $P_{\mathrm{F}} = 4/(3\sqrt{3}) \approx 0.77$ for a Lorentzian profile, $\Delta\nu$ the linewidth, C the contrast, and R the detected photon rate. η_{PSN} can be improved by minimizing the linewidth and maximizing the values of contrast and detected photon rate. Here, the interplay between the optical pumping process and the microwave spin manipulation needs to be considered to optimize η_{PSN}. This interplay strongly depends on the used diamond material and the resulting spin–lattice relaxation time T_2^* of the NV ensembles. In general, the optical pumping rate and the microwave drive should be comparable to $1/T_2^*$ to exploit the dynamics of the NV ensembles properly.[10,11] The main extrinsic parameters limiting the sensitivity of a NV magnetometer are thus the optical power, the power of the applied microwave field, and the fluorescence collection efficiency.[11,13] Both linewidth and contrast are affected by microwave and optical power, whereas the collection efficiency results from the design of the sensor. The optical power was fixed by design but was chosen to closely fulfill an optical pumping rate that is comparable to $1/T_2^*$. A detailed analysis of the adjustable parameters of our NV sensor with impact on the sensitivity will be given in Section 3.

The sensor head of the integrated NV magnetometer is shown in **Figure 2** and the complete experimental setup can be seen in Figure S1 of the Supporting Information. The integrated sensor head includes a diamond with NV centers, which is connected to a lens and an optical single mode fiber, a microwave (MW) circuit for providing an oscillating magnetic field necessary for the spin manipulation, and a printed circuit board (PCB) containing two photodiodes for a balanced detection scheme of the emitted fluorescence and the excitation laser light. Microwave source and laser were located externally and connected to the sensor head by radiofrequency cables and an optical fiber, respectively.

We used a fiber coupled, compact laser module from Q.ANT GmbH with an emitting wavelength of 521.9 nm (dimensions of the laser module: 35 × 110 × 115 mm³) providing 23.5 mW at the end of the fiber. This laser is coupled to a polarization-maintaining single mode optical fiber (Thorlabs PM-S405-XP, core diameter 3.0 µm, NA = 0.12). A direct connection between fiber and diamond would result in an inhomogeneous optical excitation of the NV centers along the optical path, see Figure S2a of the Supporting Information. We used therefore a gradient refractive index (GRIN) rod lens (GRINTECH GT-LFRL-050-025-50-NC (670), NA = 0.5) to collimate the light that exits the fiber before it enters the diamond, see Figure S9b of the Supporting Information. The GRIN rod lens and fiber were connected by an epoxy glue and inserted into a pigtailed glass ferrule to stabilize the assembly. The diamond was directly glued to the surface of the GRIN lens with a droplet of polydimethylsiloxane.

We used a (111)-oriented plate with dimensions of 0.8 × 0.8 × 0.5 mm³ obtained by laser-cutting and polishing from a 99.97 % ^{12}C enriched diamond single crystal grown by the temperature gradient method at high pressure and high temperature conditions. The original crystal was irradiated with 2 MeV electrons (2×10^{18} cm^{-2}) at room temperature and annealed at

1000 C for 2 h in vacuum resulting in the concentrations of [NV$^-$] ≈ 0.4 ppm and [P1] ≈ 2.0 ppm measured by electron spin resonance (ESR).

For the microwave-based spin manipulation, we used a double split-ring resonator (Figure S9, Supporting Information) formed by two inductively coupled transmission lines, which were terminated by two capacitive gaps, in order to provide a microwave field of sufficient amplitude.[26] The resonator was fabricated on a 640 µm thick Rogers RO3010 substrate with a copper metallization of 20 µm on both sides (PCB dimensions of $15 \times 24.5 \times 0.72$ mm³). An MMCX connector was used to supply the resonator with microwave power, transferred by a 50 Ω microstrip line coupled to the double split-ring resonator. The bandwidth of the resonator is 23.48 ± 0.08 MHz and the resonance frequency can be tuned in the range from 2.8 to 3.0 GHz by putting a metallized plate (resonator tuning stick, Figure 2) on the resonator structure. Further details of the microwave resonator will be given in Section S10 of the Supporting Information.

Microwaves in the GHz frequency range were delivered by a compact local oscillator (Windfreak Synth USB II) with an output power of 3 dBm and a fixed frequency. Additionally, we used a second source (RedPitaya STEM 125-14 V1.0) to synthesize the baseband in the MHz frequency range. The baseband signal was pre-amplified using a low noise amplifier (Mini-Circuits ZFL-1000LN+). Both signals were subsequently mixed using a low conversion loss mixer (Mini-Circuits ZFM-4212+) and amplified using three low noise microwave amplifiers (Mini-Circuits ZX60-P33ULM+) with a gain of 8.8 dB each (at a frequency of 3.0 GHz). The frequency of the baseband signal was modulated with a modulation frequency f_{mod} and a modulation depth f_{depth}, i.e., $f_{\mathrm{BB}}\ (t) = f_{\mathrm{BB}}\ + f_{\mathrm{depth}}\ \cdot \sin(2\pi f_{\mathrm{mod}} t)$, where f_{BB} is the mean frequency of the baseband. This signal was mixed with the fixed frequency f_{LO} of the local oscillator resulting in the overall mean frequency $f_{\mathrm{c}} = f_{\mathrm{LO}}\ + f_{\mathrm{BB}}$.[27] The following analysis will refer to f_{c}. For an enhancement of the magnetic sensitivity we simultaneously applied three mean frequencies $f_{\mathrm{c}}, f_{\mathrm{c}} - f_{\mathrm{HFS}}$, and $f_{\mathrm{c}} + f_{\mathrm{HFS}}$ in order to address all three ^{14}N hyperfine resonances with a frequency splitting f_{HFS} of 2.16 MHz simultaneously.[19,28] In the following, we will label such measurements with "3 HFS on", while "3 HFS off" means that only the mean frequency f_{c} is applied. If not explicitly mentioned, the default settings for the presented results is "3 HFS on" and the given values will refer to the total power of the three frequencies.

The fluorescence emitted by the diamond was collected by a photodiode (PD) located on the diamond surface opposite to the fiber and GRIN lens, see Figure 2a. This is in contrast to previous publications, where the fiber was used both for optical excitation and fluorescence collection.[29–32] For this purpose, we used a chip photodiode (Hamamatsu S12915-33CHIP) with a photosensitive area of 2.4×2.4 mm² and a responsivity of $R_{670\ \mathrm{nm}} \approx 0.54$ A W^{-1} (at 670 nm wavelength). A 1.45 µm thin distributed Bragg reflector (DBR) grown by chemical vapor deposition of several layers of amorphous silicon carbide (aSiC, $n \approx 2.6$) and silicon oxide (SiO$_2$, $n \approx 1.5$) was deposited on the surface of the photodiode acting as a long-pass filter to block the laser excitation light.[18] Besides the sole detection of the emitted fluorescence of the NV centers, we additionally monitored the laser intensity by a second photodiode with responsivity of $R_{522\mathrm{nm}} \approx 0.40$ A W^{-1}. This photodiode was positioned next to the first photodiode on the common PCB and was coated with a customized DBR blocking the fluorescence light (short-pass filter), see Figure 2a. Both photodiodes were reverse biased with a voltage of 6 V. In contrast to Kim et al., the distance between the microwave circuit and the photodiodes was rather large (≈ 1.0 mm) such that eddy currents in the photodiodes caused by the microwave play only a minor role.[22] Implementing long cut holes on the photodetection board enabled a variable alignment of the photodiodes relative to the position of the diamond, such that the ratio of detected fluorescence and laser (reference) signal can be adjusted. Here, our design represents a compromise between full detection of the fluorescence signal and maintaining the ability of balanced detection. For this purpose, the signals of the two photodiodes were fed to a logarithmic transimpedance amplifier (Texas Instruments LOG114), whose preamplified output was digitized and demodulated (according to the applied modulation frequency) by the analog-to-digital module of the RedPitaya (14 bit, 125 MSamples s^{-1}). The demodulated signal S_{demod}, shown in **Figure 3**a, indicates the peak-to-peak amplitude of a signal oscillating at the carrier frequency f_{mod}.

For the experiments, we used the technique of ODMR to measure magnetic fields. Therefore, the demodulated signal output S_{demod} of the RedPitaya resembles to the derivative of the typical Lorentzian profile of the ODMR spectrum. Close to the resonance frequency, S_{demod} is proportional to the detuning Δf from the corresponding resonance frequency $f_{\pm}$ (Figure 3a). We extracted information about the linewidth $\Delta\nu$ and contrast C of the electron spin resonance by integrating the demodulated signal S_{demod} and fitting the resulting data S_{integ} to a Lorentzian function $g(x)$ of

$$g\ (x) = A \frac{(\Delta\nu/2)^2}{\left(x - x_0\right)^2 + (\Delta\nu/2)^2} \tag{3}$$

where A is an amplitude factor linked to spin contrast C, $\Delta\nu$ is the full width at half maximum of the resonance curve, and x_0 is the resonance frequency (see Figure 3b). Details of the signal processing, including the signal integration and the determination of the contrast, are summarized in Section S4 of the Supporting Information.

In order to spectrally separate the four NV orientations and hyperfine splittings, we used a self-constructed, current carrying Helmholtz coil, which is a necessary functional part of the sensor head. The Helmholtz coil consists of 35 windings on each side providing an offset magnetic field of ≈ 1.07 mT at a current of 0.5 A. The windings were designed in a tapered shape to fulfill the Helmholtz coils' condition, i.e., the distance between the two coils equals the radius of the coils, resulting in field deviations of less than 0.1 % inside the volume of the diamond, see Figure S3 of the Supporting Information. A diameter of 22.5 mm for the smallest winding and a diameter of 36.2 mm for the largest winding were used.

3. Experimental Results

An ODMR spectrum of the NV ensembles recorded with an offset magnetic field generated by the tapered Helmholtz coil is

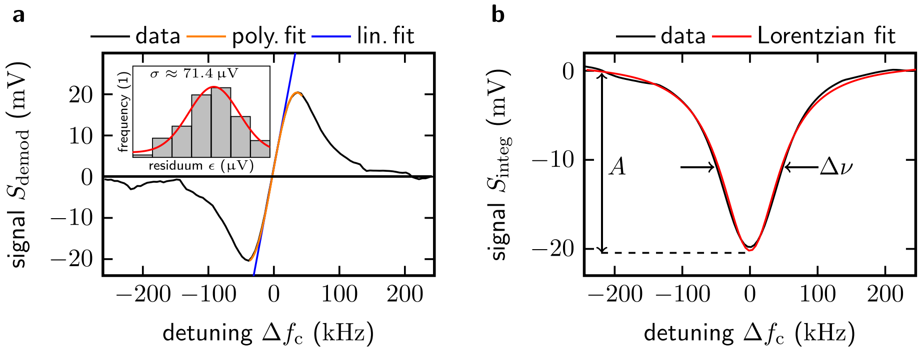

Figure 3. Demodulated and integrated signal of an ODMR spectrum. a) The recorded signal S_{demod} (black curve) is shown as a function of the detuning Δf_c from the resonance frequency, which is characterized by the zero-crossing of the signal. A polynomial of 6th order (orange curve) was applied as empirical fit to the data to determine the slope parameter at the zero-crossing. The blue curve shows the linear contribution of the polynomial. The noise parameter was derived by the standard deviation σ of the residuum ϵ that results from subtracting the polynomial fit values from the data, which are summarized in a histogram. b) Integrating S_{demod} resembles the resonance curve S_{integ} (black curve) with a Lorentzian shape (fit red curve) with $\Delta\nu$ the linewidth and A the amplitude of the resonance linked to contrast C.

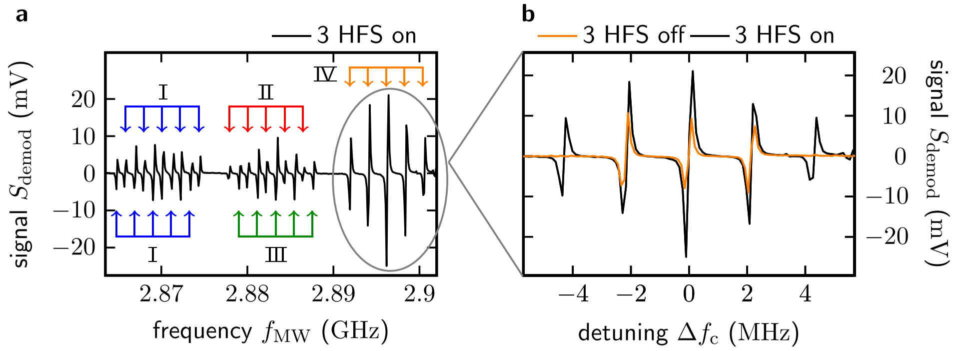

Figure 4. Optically detected magnetic resonance (ODMR). a) Spectrum of the measured demodulated signal S_{demod} showing spin transitions from the $m_s = 0$ to $m_s = 1$ states including hyperfine interactions. The spectrum was recorded at a modulation frequency of 5 kHz and a modulation depth of 100 kHz with 40 ms integration time. The total microwave power was 0.91 mW with a simultaneous excitation of the three hyperfine split transitions. Each NV axis produces five characteristic zero-crossings resulting from the simultaneous manipulation of the ^{14}N hyperfine splitting, which are labelled with colored arrows and Roman letters. An exception is orientation I, where the transitions from $m_s = 0$ to $m_s = \pm 1$ overlap around $D_{\text{gs}} \approx 2.87$ GHz, so that ten characteristic crossings are visible. b) Detailed view of the measured resonances of the NV orientation with the largest magnetic field projection with a comparison of the applied microwave manipulation: "3 HFS on" (black curve) and "3 HFS off" (orange curve).

shown in **Figure 4**a. The measured demodulated signal S_{demod} shows the spin transitions from the $m_s = 0$ to $m_s = 1$ states including the three sublevels that result from the hyperfine interaction with the nuclear spin of the ^{14}N isotope. All four possible orientations contribute to the spectrum depicted in Figure 4a. The color-coded arrows are related to the electron spin resonances of the four NV orientations. Due to the simultaneous manipulation of the three hyperfine splittings, five characteristic zero-crossings can be observed in Figure 4a for each NV axis. In order to show the increase in signal amplitude due to the simultaneous hyperfine spin manipulation in comparison to a standard spin manipulation, we plotted the spectra in a common plot superimposed, see Figure 4b. The simultaneous excitation of the three ^{14}N hyperfine split transitions should result in a threefold increase of the contrast. However, we only find a factor of ≈2.61 larger amplitude, which may be due to an uneven power level of the combined three mean microwave frequencies, i.e., f_c, $f_c - f_{\text{HFS}}$, and $f_c + f_{\text{HFS}}$, see Figure S5a of the Supporting Information.

As mentioned above, it is essential to evaluate the interplay between optical excitation and spin manipulation to find the optimal working point for our NV magnetometer. We used the measured curve of the ESR, which corresponds to the NV orientation with the largest field projection, as the basis for this analysis to improve the sensor's performance. As depicted in Figure 4a, the mean frequency f_c was swept to record an ODMR spectrum of the demodulated signal S_{demod}. We applied a polynomial fit of 6th order to the measured data of S_{demod} to evaluate the linear slope m at the zero-crossing as well as to obtain information about the noise on the measured signal. The noise was calculated as the standard deviation σ of the residuum ϵ that results from subtracting the polynomial fit from the measured data, see Figure 3a. Using these quantities and the gyromagnetic ratio of the NV centers, we approximated the sensitivity for a measurement time t_{int} in the linear range close to the zero-crossing point of S_{demod} with

$$\eta_B = \frac{\sigma}{\gamma_{\text{NV}} \cdot m} \sqrt{t_{\text{int}}}\,. \tag{4}$$

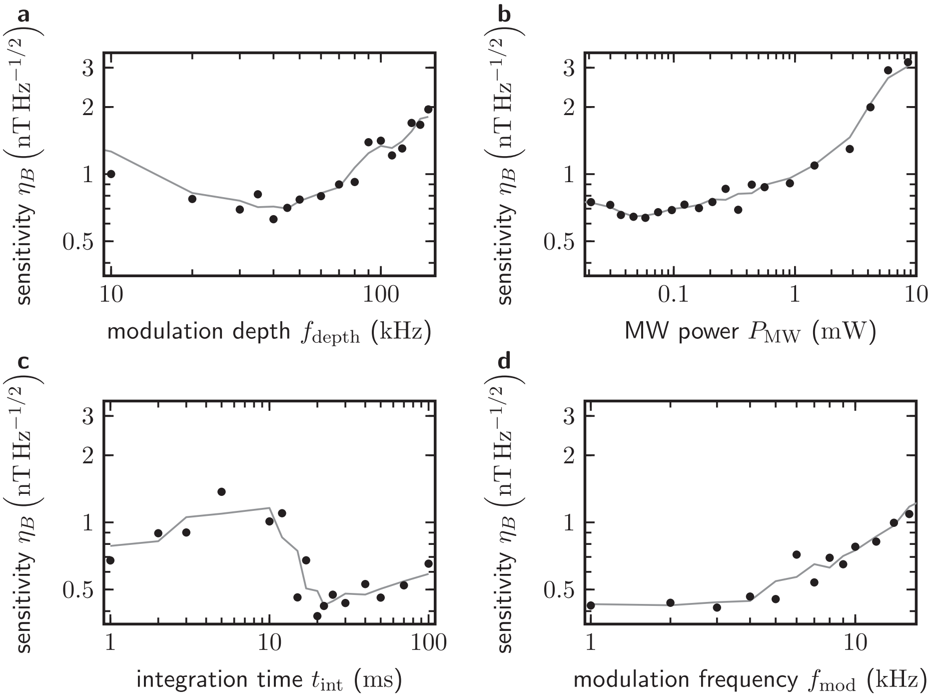

Figure 5. Evaluation of the magnetic field sensitivity with respect to sensor parameters. The sensitivity was evaluated on the NV orientation with the largest field projection, i.e., NV orientation IV in Figure 4a. The gray line corresponds to a moving mean of three neighboring data points and is added to the graphs as a guide to the eye. a) Variation of the modulation depth f_{depth} at a microwave power of 16 µW, 1 kHz modulation frequency for an integration time of 1 ms. b) Variation of the microwave power P_{MW} at 1 kHz modulation frequency and 40 kHz modulation depth for an integration time of 1 ms. c) Variation of the integration time t_{int} at a microwave power of 58 µW, 1 kHz modulation frequency, and 40 kHz modulation depth. d) Variation of the modulation frequency f_{mod} at a microwave power of 58 µW and 40 kHz modulation depth for an integration time of 20 ms.

In the following, we evaluated the optimal working point of our NV sensor in order to improve the sensitivity η_B by varying the adjustable parameters, i.e., modulation depth f_{depth}, microwave power P_{MW}, integration time t_{int}, and modulation frequency f_{mod}, while the laser power was fixed by design in order to achieve an optimal pumping rate that is close to $1/T_2^*$. The results of this optimization analysis are summarized in **Figure 5**. The power of the laser module of 23.5 mW corresponds to an estimated average optical intensity of $I_{\mathrm{opt}} \approx 390\ \mathrm{W\,cm^{-2}}$ (along the optical path inside the diamond, for further details see Section S10, Supporting Information). Based on the results by Dréau et al. and Levine et al., this value of the optical intensity corresponds to the excitation regime where the tradeoff between high contrast and small linewidth results in an optimal value for the sensitivity.[10,13]

First, we studied the dependence of the modulation depth f_{depth} on the sensitivity, as shown in Figure 5a. El-Ella et al. found an optimal modulation depth, which maximizes the measured slope m, corresponding to half of the resonance linewidth.[33] The extracted slope reached a maximum at 40 kHz modulation depth, whereas the noise showed no clear trend on the modulation depths, see Figure S8c of the Supporting Information. Fitting the data of S_{integ} with the Lorentzian function from Equation (3) a linewidth of 81.8 ± 2.4 kHz and a contrast of $0.43\% \pm 0.01\%$ were extracted for $f_{\mathrm{depth}} =$ 40 kHz (Figure S8b, Supporting Information), which is in good agreement to the findings of El-Ella et al.[33] Therefore, $f_{\mathrm{depth}} =$ 40 kHz was chosen for the following measurements.

In a second step, the influence of the applied microwave power was evaluated. We observed an increase of the measured linewidth for microwave powers larger than 0.1 mW (Figure S9b, Supporting Information) due to power broadening.[10] For microwave powers below 0.1 mW, the linewidth seems to be unaffected by power broadening. We extracted an inhomogeneously broadened linewidth $\Delta\nu_{\mathrm{inh}}$ of ≈76.47 kHz by applying a theoretical model of the linewidth of NV ensembles according to Jensen et al. to the measured data, see Figure S9b of the Supporting Information.[34] Regarding the measured contrast that results from the simultaneous excitation of the three hyperfine levels, a maximum value of ≈ 1.0 % is achieved for $P_{\mathrm{MW}} \approx 1.45$ mW. However, for applied powers above 1.45 mW the contrast deteriorated as microwave induced power broadening dominated over the optical pumping rate and became major linewidth determining factor. We found that the slope was largest for a moderate microwave power of ≈ 58 µW. The noise had a similar dependence on the microwave power. As a result, the overall sensitivity showed a rather weak dependence on the evaluated power range from 0.02 to 0.2 mW.

In the third step, we varied the integration time based on the optimal parameters to date to record slope and noise. The best value for the sensitivity was obtained for an integration time of 20 ms, see Figure 5c, which is linked to the 50 Hz main frequency of the European power lines. The measured values of slope and noise are shown in Figure S10a of the Supporting Information.

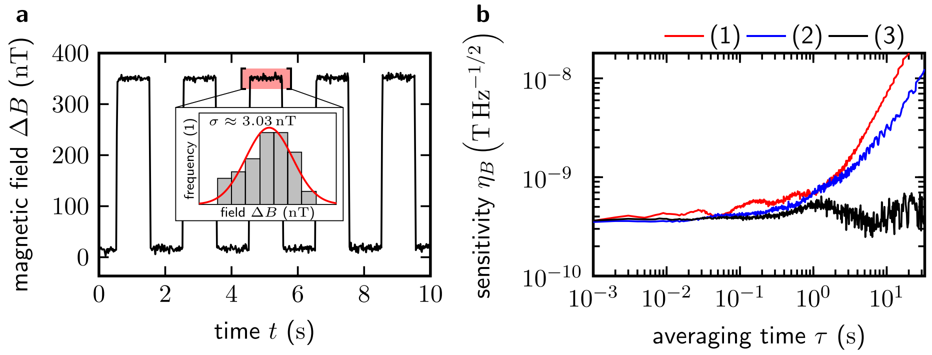

Figure 6. Sensitivity determination with square-wave test field using the Allan deviation. a) The demodulated signal S_{demod} was recorded for 10 s with an integration time of 20 ms per data point. A test magnetic field was applied with a square-wave function of 2 Hz and amplitude of 2.18 mA on the copper windings around the pair of Helmholtz coils corresponding to an induced magnetic field of 333 nT and is clearly visible in the recorded data trace (black curve). The noise on a single 1 s step was evaluated by the standard deviation of a Gaussian distribution ($\sigma \approx 3.03$ nT, red curve) on the recorded data and extrapolates to 429 pT Hz$^{-1/2}$ for 20 ms integration time. b) Magnetic field sensitivity derived by analyzing the Allan deviation $\sigma_{\mathrm{A}}(\tau)$ of recorded time traces (without applying any magnetic test field). The data of (1) and (2) are based on time traces of magnetically sensitive cases, where the applied microwave field was set to the point of zero-crossing in the demodulated spectrum. In (2) the NV sensor was totally enclosed in the magnetic shielding of two half-shells made of mu-metal, for details see main text, whereas in (1) the sensor was unshielded. In (3) the magnetically insensitive data are shown without using any shielding. The time traces were recorded with a sampling rate of 1 kHz and a simultaneous manipulation of the three hyperfine states was applied in all measurements.

In the fourth step, the modulation frequency was varied under the parameters determined so far, see Figure 5d. We found a maximum slope for ≈ 1 kHz modulation frequency, see Figure S7b of the Supporting Information. While the slope decreased for $f_{\mathrm{mod}} > 1$ kHz, the noise level was almost constant for all investigated values of f_{mod}, see Figure S11c of the Supporting Information. Modulation frequencies smaller than 1 kHz resulted in a decreased slope, which can be understood by the used high-pass filter in our photodetection circuit, see Figures S6 and S7b of the Supporting Information. The measured values of linewidth and contrast of the modulation frequency variation are summarized in Figure S11b of the Supporting Information. The contrast resembled the behavior of the slope and decreased as the modulation frequency was increased, see Figure S11a of the Supporting Information. A maximum contrast of 0.62 % was obtained for $f_{\mathrm{mod}} = 1$ kHz. The linewidth showed a slight increase up to a modulation frequency of 10 kHz; for larger f_{mod} the linewidth broadened significantly. Here, we note that the resulting shape of the measured signal significantly deviated from a Lorentzian profile for $f_{\mathrm{mod}} > 16$ kHz such that the linewidth and contrast of the electron spin resonance cannot be extracted correctly. We will refer to this behavior in Section 4.

Based on the described method of slope and noise characterization the best measured sensitivity was ≈ 424 pT Hz$^{-1/2}$, which was achieved for a frequency modulation and simultaneous excitation of the three hyperfine interactions with $f_{\mathrm{depth}} = 40$ kHz, $P_{\mathrm{MW}} = 58$ µW, $t_{\mathrm{int}} = 20$ ms, and $f_{\mathrm{mod}} = 1$ kHz, see Figure 5d.

The magnetic sensitivity of the sensor device was further evaluated using a magnetic shielding. For this purpose, we put a 180 mm diameter end cap of a mu-metal shield (Twinleaf MS-2) on top of the sensor and characterized the magnetic sensitivity with the method described above. We measured a sensitivity of 369 pT Hz$^{-1/2}$ for this partial enclosure of the NV sensor. A further reduction of the measured sensitivity was achieved by a complete enclosure of the NV sensor using two shielding end caps resulting in a sensitivity to 344 pT Hz$^{-1/2}$. This is an improvement of factor 1.23 compared to the unshielded setting.

Besides the determination of the magnetic sensitivity by taking the measured parameters of slope and noise of the demodulated signal at the zero-crossing point, we further evaluated the sensor performance under the application of a test magnetic field. A copper wire was wound around the pair of Helmholtz coils, on which a signal with square-wave function of 2 Hz frequency and amplitude of 2.18 mA was applied by an arbitrary waveform generator (Agilent 33220A). The applied signal corresponds to an induced magnetic field of ≈ 333 nT with a field orientation parallel to the applied offset magnetic field; a detailed description of the generated test field is summarized in Section S11 of the Supporting Information. We analyzed the sensitivity by recording the demodulated signal as a time trace under the application of the test field, see **Figure 6**a. Each data point of the recorded time trace corresponds to an integration time of $t_{\mathrm{int}} = 20$ ms. The noise on a single 1 s step was evaluated by fitting the histogram of the recorded data set with a Gaussian distribution. Indicating a standard deviation σ of ≈ 3.03 nT, this measurement extrapolated to a sensitivity of $\sigma \cdot \sqrt{t_{\mathrm{int}}} \approx 429$ pT Hz$^{-1/2}$.

The sensor performance was further analyzed by recording time traces of magnetic stimuli, i.e., the microwave frequency was set to the zero-crossing, and by calculating the Allan deviation σ_{A} of this data. In general, the Allan deviation determines the deviation of the measured data binned to intervals with averaging length τ.[35] In contrast to the standard deviation, the Allan deviation analyzes data sets depending on the averaging time τ and thus providing time dependent noise information. The Allan variance $\sigma_{\mathrm{A}}^2(\tau)$ is calculated by[2]

$$\sigma_{\mathrm{A}}^2\ (\tau) = \frac{1}{2}\left\langle \left(\bar{y}_{n+1} - \bar{y}_n\right)^2 \right\rangle \tag{5}$$

where $\bar{y}_n$ and $\bar{y}_{n+1}$ are the mean values of two consecutive intervals of length τ. The calculated values of the Allan deviation were adjusted by the slope m to translate deviations in the measured signal into magnetic field deviations, see Figure 6b. We additionally enclosed the NV sensor using the magnetic shielding of two mu-metal half-shelves, as described above, to evaluate the influence of surrounding magnetic noise sources on the achievable sensor. The noise of a magnetically insensitive case was additionally measured without using any magnetic shielding. For this purpose, we applied a microwave frequency with 19.45 MHz detuning from the selected resonance frequency.

For short averaging times τ in the range of 1–100 ms, the mean sensitivity level of the magnetically sensitive measurement was improved from 440 to 396 pT $\text{Hz}^{-1/2}$ through introducing the shielding. Considering a 20 ms integration time derived by the optimization steps, the unshielded measurements revealed a sensitivity of 436 and 365 pT $\text{Hz}^{-1/2}$ was achieved for the shielded measurement environment. The shielded measurements showed a flat behavior for 1–100 ms comparable to the magnetically insensitive measurement, whereas the sensor in the unshielded environment varied in its sensitivity result. An increase in the measured sensitivity for both settings was observed for time scales larger than 100 ms. Here, we note that we observed fluctuations in the data from measurement to measurement for the unshielded setting, which may be due to magnetic fields that prevail in the background.

The logarithmic balancing of the two photodiodes prevented noise measurements of the detection output without laser and microwave excitation such that the contribution of electronic noise to the overall sensitivity cannot be solely analyzed. A noise floor of ≈ 364 pT $\text{Hz}^{-1/2}$ was characterized for 1 ms integration time recorded by the magnetically insensitive measurement, see Figure 6b, indicating a lower limit of the achievable sensitivity of our device.

As an application, we used the NV sensor to measure the change in magnetic field ΔB due to the movement of an elevator, see **Figure 7**. For this purpose, we positioned the NV sensor roughly 4 m away from the doors of an elevator in the third floor. The NV magnetometer recorded the movement of the elevator by tracking the resonance frequency of the selected spin transition using a feedback loop to adjust the applied microwave frequency. From the measured change in magnetic field, shown in Figure 7, it can be clearly identified when the elevator started with the upward movement (observed by an increase of the field change), opened its doors (by an additional increase of the field change compared to the “standing” case at the third level), and waiting period in this upper level. The closing of the doors, the downward movement, as well as the repeated opening of the doors were detected by the sensor in the form of a decreasing change decreasing ΔB compared to the starting situation.

4. Discussion and Outlook

For the evaluation of the achieved sensor performance, it is essential to have a look on its fundamental limit. Due to the optical readout of the spin states, the NV magnetometer is limited by photon shot-noise given by Equation (2). To calculate η_{PSN}, we determined the photon rate from the average photocurrent $I_{\text{PD}_{\text{fl}}}$ by measuring the voltage U_{shunt} drop at a $R_{\text{shunt}} = 10\,\Omega$ shunt resistor. For a measured U_{shunt} of 0.40 mV the photon rate $R = \frac{I_{\text{PD}_{\text{fl}}}}{e} = \frac{U_{\text{shunt}}}{R_{\text{shunt}} \cdot e}$ results in $\approx 2.47 \times 10^{14}$ Hz with e being the elementary charge. Using Equation (2) and the measured linewidth of 92.19 kHz and contrast of 0.62 % the photon shot-noise limited sensitivity is ≈ 26 pT $\text{Hz}^{-1/2}$. This value is a factor of ≈ 13 smaller than the best measured sensitivity of ≈ 344 pT $\text{Hz}^{-1/2}$. Regarding this discrepancy a factor of $\sqrt{2} \approx 1.41$ can be explained by the usage of the balanced photodetection unit based on two single independent photodiodes compared to a single-photodiode-usage. Further deviations may arise from fluctuations of the laser and its interplay with the limited common mode rejection of the balanced photodetector module. For time scales ≥ 1 s, the observed magnetic field noise is possibly due to power fluctuations of the laser associated with temperature variations of the diamond (for further details see Section S12, Supporting Information).

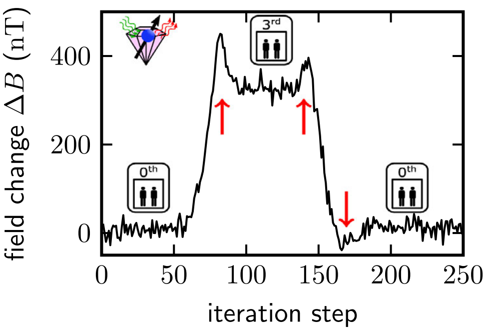

Figure 7. Measurement of the change in the magnetic field due to the movement of an elevator. The NV magnetometer was positioned roughly 4 m away from the doors of an elevator three floors above the ground floor. For tracking the resonance condition of the selected NV transition, the demodulated signal S_{demod} was used as an error signal for a feedback loop to adjust the applied microwave frequency. The microwave frequency was adjusted by 250 Hz corresponding to a magnetic field change of 8.92 nT. We recorded S_{demod} for 1 ms integration time (per iteration step) with the following experimental parameters: 1 kHz modulation frequency, 40 kHz modulation depth, and 58 μW microwave power. In this measurement, the elevator started in the ground floor and moved to third level, opened and closed its doors, and moved then down to the ground floor. The red arrows indicate the impact of opening and closing the elevator’s doors.

Finding the optimal working point of the NV magnetometer by optimizing the relevant operation parameters is essential to obtain a highly sensitive device at efficient usage of the sensor power supply. Due to the interplay between optical and microwave excitation it may be possible that altering the applied laser power improves the sensitivity. The performed 1D parameter sweeps might result in a local optimum of the sensitivity, which can be potentially further improved. We further note that the parameter evaluation of the modulation frequency was not straight forward compared to the parameter sweeps of microwave power and modulation depth. This is mainly linked to the implemented high-pass filter in the transimpedance amplification circuit of the balanced detection unit. Based on simulations of the electronic circuit using LTspice®, we expected the output of the logarithmic transimpedance amplification circuit to show a flat behavior over a frequency range between 1 and 50 kHz, see Figure S6 of the Supporting Information. However, experimental results of the contrast and slope determination revealed a maximum value at 1 kHz modulation frequency, as depicted in

Figure S7b of the Supporting Information. The measured signal deteriorated for higher modulation frequencies, which can be explained by a relatively small optical pumping rate compared to the modulation frequency of the microwave. We estimated the pumping rate to be ≈ 32 kHz (see Section S10, Supporting Information), so that under these conditions the pumping of the NV system is too slow to follow the fast modulation resulting in a reduced signal. In the simulation, the dynamics of the NV centers was neglected. Therefore, we assume that the discrepancy between experimental observation and simulative prediction results from the complex excitation dynamics of the NV centers.

The method of applying an additional magnetic test field to the NV sensor and measuring the noise on the demodulated signal at the point of zero-crossing, i.e., resonance condition, confirmed the sensitivity that was obtained from the analysis of the slope and its residuum, see Figure 3a. For short averaging times in the range of 1–100 ms the achievable sensitivity varied, which may be due to (magnetic) noise/fluctuations in the sensor's environment. The analysis of the Allan deviation revealed that the performance worsened for sensing times exceeding 1 s independent on the sensor's environment, i.e., unshielded and magnetically shielded. Observed drifts in the recorded time traces may be linked to temperature variations and need to be mitigated to improve both the sensor's sensitivity and stability on larger time scales. Recent publications have shown how to set up a sensor with temperature invariance by simultaneously addressing both transitions from the $m_s = 0$ to $m_s = \pm 1$, i.e., making use of double quantum magnetometry.[36,37] A complete enclosure of the NV magnetometer in a magnetic shielding showed an improvement of the sensitivity.

The fluorescence collection efficiency could be further optimized, as we detected less than one percent of the power that was used for excitation (a calculated fluorescence power of 73.1 µW based on the detected photocurrent for a fluorescence wavelength of 670 nm and an estimated excitation output power at the GRIN lens of 18.3 mW). This low fluorescence collection efficiency originates from the small solid angle of the photodetector seen from the fluorescing diamond. While the geometric center of the diamond was located above the photodiode used to detect the reference signal from the laser, only the share of the fluorescence that was emitted laterally to the side of the other photodetector ($\mathrm{PD_{fl}}$) was detected, see Figure 2a. The DBR filters deposited on the surface of the photodiode further reduced the detectable fluorescence intensity as these filters showed a transmission of ≈ 78 %. An instant improvement in the fluorescence detection efficiency could be achieved by avoiding the step in refractive index between the diamond and the photodiode by filling the gap with a material having a larger refractive index than air. This could mitigate the problem of total internal reflections of the emitted fluorescence due to diamond's high refractive index.

A further improvement of sensor performance could be achieved by equalizing the microwave power levels at the three hyperfine frequencies, since different power levels prevent a full exploitation of simultaneously addressing hyperfine levels.

Besides the implementation of temperature invariance of the NV sensor, another possibility to enhance the achievable sensitivity could be the use of flux concentrators, as recently shown by Fescenko et al., which collect the magnetic flux from a large area and direct it to the NV sensor.[14] The use of such concentrators must nevertheless be viewed critically from the point of view of the intended application, as any restrictions on the use of the sensor could be associated with the use of these concentrators, e.g., for a vector magnetometry application.

Setting up the sensor device as a vector magnetometer, we would need to implement a simultaneous addressing of at least three NV orientations in the microwave and signal processing circuitry.[16] Tracking fast changing magnetic signals would further require a closed loop control for tracking the NV resonance frequencies. Further miniaturization for mobile applications of NV magnetometers could take advantage of using complementary metal-oxide-semiconductors as shown by Kim et al.[22]

Regarding power consumption of the NV magnetometer, the power efficiency of the microwave resonator could be further enhanced by optimizing the coupling property, e.g., by placing additional dielectric material on the coupling gap. This could reduce the need of amplification or the input power for the spin manipulation.

The compactness and portability of our NV magnetometer was designed to pave the way for a wide range of applications including GPS-free navigation on earth and space missions as well as the detection of biomagnetic signals, e.g., for magnetocardiography and magnetoencephalography.[17] By implementing the above mentioned measures, the sensor's sensitivity could be improved to the required level of $\approx 10\ \mathrm{pT\ Hz^{-1/2}}$ for magnetocardiography. In addition, our NV magnetometer could be used for the detection of electric currents, e.g., for battery diagnostics.

To classify our NV sensor in terms of sensitivity and level of integration, we summarized recent results both for NV diamond magnetometers as well as for OPMs in **Table 1**. Some experiments with NV centers and OPMs have outperformed our work in terms of sensitivity. However, regarding these NV experiments, the results have been achieved with laboratory equipment, such as confocal microscopes, limiting their usability for portable applications. Considering OPMs, a few companies have specialized in manufacturing OPMs, which achieve sensitivities $< 20\ \mathrm{pT\ Hz^{-1/2}}$ and can be used for mobile applications. Further comparing our work to recently demonstrated integrated NV sensors, our work shows both advances in performance with sub-$\mathrm{nT\ Hz^{-1/2}}$ sensitivity and increased level of integration.

Analyzing the overall power consumption, our NV magnetometer consumes ≈ 5.1 W in operation mode (excluding the power of the computer needed to control the experiments). This value is comparable to the values given in the data sheets of commercially available OPMs, see Table 1, ranging from 0.7 to 5.0 W.

5. Conclusion

In conclusion, we have demonstrated an integrated portable prototype of a magnetometer based on the NV centers in diamond. The diamond attached to an optical fiber, the microwave resonator, and a balanced detection scheme built up by two photodiodes was integrated into a compact sensor head. Our focus in setting up this prototype was put on the size and compactness of the complete sensor device while enabling high sensitivity measurements. This includes the choice of laser source, microwave equipment, and signal processing such that the sensor device can be used in real world applications outside laboratory environments. Using the frequency modulation technique

Table 1. Comparison of magnetometer technologies.

Technology	Level of miniaturization	Sensitivity	References
NV diamond magnetometer	Laboratory confocal setup	900 fT Hz$^{-1/2}$ to 30 pT Hz$^{-1/2}$	[2,12,14,38,39]
	Integrated sensor head	310 pT Hz$^{-1/2}$ to 67 nT Hz$^{-1/2}$	[19–21,23]
	Integrated sensor head	344 pT Hz$^{-1/2}$	This work
OPM	Laboratory setup	160 aT Hz$^{-1/2}$ to 5 fT Hz$^{-1/2}$	[40,41]
	Integrated sensor head	10 fT Hz$^{-1/2}$	[42]
	Commercial product	10 fT Hz$^{-1/2}$ to 20 pT Hz$^{-1/2}$	QZFMGen-2,[a)] QTFM,[b)] microSAM,[c)] microSERF[d)]

[a)] https://quspin.com/products-qzfm/ (2020/12/02); [b)] https://quspin.com/qtfm/ (2020/12/02); [c)] https://twinleaf.com/scalar/microSAM/ (2020/12/02); [d)] https://twinleaf.com/vector/microSERF/ (2020/12/02).

for measuring electron spin resonance we achieved a magnetic field sensitivity of 344 pT Hz$^{-1/2}$. We further discussed solutions to improve the sensor performance and abilities to increase the integration level.

Supporting Information

Supporting Information is available from the Wiley Online Library or from the author.

Acknowledgements

The authors thank Jens Baringhaus for the support of scanning electron microscope images of the resonator structure. The authors acknowledge financial support by the German Federal Ministry of Education and Research (BMBF) within the “BrainQSens” project (No. 13N14435) and the “MiLiQuant” project (No. 13N15062). This project has received funding from the European Union’s Horizon 2020 research and innovation program under Grant Agreement No. 820394 (ASTERIQS). In addition, the authors acknowledge the support of the Japan Society for the Promotion of Science (JSPS) KAKENHI (No. 20H00340).

Conflict of Interest

F.M.S., A.B., T.B., J.K., R.R., and T.F. are coinventors of a pending patent application related to this work. The remaining authors declare no competing financial interests.

Data Availability Statement

Research data are not shared.

Keywords

diamond, magnetometers, nitrogen vacancy centers, quantum sensing, quantum technologies

Received: September 30, 2020
Revised: December 23, 2020

[1] J. M. Taylor, P. Cappellaro, L. Childress, L. Jiang, D. Budker, P. R. Hemmer, A. Yacoby, R. Walsworth, M. D. Lukin, *Nat. Phys.* **2008**, *4*, 810.
[2] T. Wolf, P. Neumann, K. Nakamura, H. Sumiya, T. Ohshima, J. Isoya, J. Wrachtrup, *Phys. Rev. X* **2015**, *5*, 041001.
[3] P. Neumann, I. Jakobi, F. Dolde, C. Burk, R. Reuter, G. Waldherr, J. Honert, T. Wolf, A. Brunner, J. H. Shim, D. Suter, H. Sumiya, J. Isoya, J. Wrachtrup, *Nano Lett.* **2013**, *13*, 2738.
[4] F. Dolde, H. Fedder, M. W. Doherty, T. Nöbauer, F. Rempp, G. Balasubramanian, T. Wolf, F. Reinhard, L. C. L. Hollenberg, F. Jelezko, *Nat. Phys.* **2011**, *7*, 459.
[5] M. W. Doherty, V. V. Struzhkin, D. A. Simpson, L. P. McGuinness, Y. Meng, A. Stacey, T. J. Karle, R. J. Hemley, N. B. Manson, L. C. L. Hollenberg, S. Prawer, *Phys. Rev. Lett.* **2014**, *112*, 047601.
[6] D. Drung, C. Abmann, J. Beyer, A. Kirste, M. Peters, F. Ruede, T. Schurig, *IEEE Trans. Appl. Supercond.* **2007**, *17*, 699.
[7] G. Balasubramanian, P. Neumann, D. Twitchen, M. Markham, R. Kolesov, N. Mizuochi, J. Isoya, J. Achard, J. Beck, J. Tissler, V. Jacques, P. R. Hemmer, F. Jelezko, J. Wrachtrup, *Nat. Mater.* **2009**, *8*, 383.
[8] J. Achard, V. Jacques, A. Tallaire, *J. Phys. D: Appl. Phys.* **2020**, *53*, 313001.
[9] K. Beha, A. Batalov, N. B. Manson, R. Bratschitsch, A. Leitenstorfer, *Phys. Rev. Lett.* **2012**, *109*, 097404.
[10] A. Dréau, M. Lesik, L. Rondin, P. Spinicelli, O. Arcizet, J.-F. Roch, V. Jacques, *Phys. Rev. B* **2011**, *84*, 195204.
[11] J. F. Barry, J. M. Schloss, E. Bauch, M. J. Turner, C. A. Hart, L. M. Pham, R. L. Walsworth, *Rev. Mod. Phys.* **2020**, *92*, 015004.
[12] J. F. Barry, M. J. Turner, J. M. Schloss, D. R. Glenn, Y. Song, M. D. Lukin, H. Park, R. L. Walsworth, *Proc. Natl. Acad. Sci. USA* **2016**, *113*, 14133.
[13] E. V. Levine, M. J. Turner, P. Kehayias, C. A. Hart, N. Langellier, R. Trubko, D. R. Glenn, R. R. Fu, R. L. Walsworth, *Nanophotonics* **2019**, *8*, 1945.
[14] I. Fescenko, A. Jarmola, I. Savukov, P. Kehayias, J. Smits, J. Damron, N. Ristoff, N. Mosavian, V. M. Acosta, *Phys. Rev. Res.* **2020**, *2*, 023394.
[15] B. Zhao, H. Guo, R. Zhao, F. Du, Z. Li, L. Wang, D. Wu, Y. Chen, J. Tang, J. Liu, *IEEE Magn. Lett.* **2019**, *10*, 8101104.
[16] J. M. Schloss, J. F. Barry, M. J. Turner, R. L. Walsworth, *Phys. Rev. Appl.* **2018**, *10*, 034044.
[17] M. W. Dale, G. W. Morley, arXiv:1705.01994, **2017**.
[18] F. M. Stürner, A. Brenneis, J. Kassel, U. Wostradowski, R. Rölver, T. Fuchs, K. Nakamura, H. Sumiya, S. Onoda, J. Isoya, F. Jelezko, *Diamond Relat. Mater.* **2019**, *93*, 59.
[19] J. L. Webb, J. D. Clement, L. Troise, S. Ahmadi, G. J. Johansen, A. Huck, U. L. Andersen, *Appl. Phys. Lett.* **2019**, *114*, 231103.
[20] D. Zheng, Z. Ma, W. Guo, L. Niu, J. Wang, X. Chai, Y. Li, Y. Sugawara, C. Yu, Y. Shi, X. Zhang, J. Tang, H. Guo, J. Liu, *J. Phys. D: Appl. Phys.* **2020**, *53*, 155004.
[21] R. L. Patel, L. Q. Zhou, A. C. Frangeskou, G. A. Stimpson, B. G. Breeze, A. Nikitin, M. W. Dale, E. C. Nichols, W. Thornley, B. L. Green, M. E. Newton, A. M. Edmonds, M. L. Markham, D. J. Twitchen, G. W. Morley, *Phys. Rev. Appl.* **2020**, *14*, 044058.

[22] D. Kim, M. I. Ibrahim, C. Foy, M. E. Trusheim, R. Han, D. R. Englund, *Nat. Electron.* **2019**, *2*, 284.
[23] S. Maayani, C. Foy, D. Englund, Y. Fink, *Laser Photon. Rev.* **2019**, *13*, 1900075.
[24] T. Plakhotnik, *Curr. Opin. Solid State Mater. Sci.* **2017**, *21*, 25.
[25] A. Gruber, A. Dräbenstedt, C. Tietz, L. Fleury, J. Wrachtrup, C. v. Borczyskowski, *Science* **1997**, *276*, 2012.
[26] K. Bayat, J. Choy, M. Farrokh Baroughi, S. Meesala, M. Lončar, *Nano Lett.* **2014**, *14*, 1208.
[27] Z. Ma, S. Zhang, Y. Fu, H. Yuan, Y. Shi, J. Gao, L. Qin, J. Tang, J. Liu, Y. Li, *Opt. Express* **2018**, *26*, 382.
[28] S. Ahmadi, H. A. R. El-Ella, J. O. B. Hansen, A. Huck, U. L. Andersen, *Phys. Rev. Appl.* **2017**, *8*, 034001.
[29] D. Duan, V. K. Kavatamane, S. R. Arumugam, G. Rahane, Y.-K. Tzeng, H.-C. Chang, H. Sumiya, S. Onoda, J. Isoya, G. Balasubramanian, *Appl. Phys. Lett.* **2018**, *113*, 041107.
[30] I. Fedotov, L. Doronina-Amitonova, A. Voronin, A. Levchenko, S. Zibrov, D. Sidorov-Biryukov, A. Fedotov, V. Velichansky, A. Zheltikov, *Sci. Rep.* **2014**, *4*, 5362.
[31] A. K. Dmitriev, A. K. Vershovskii, *J. Opt. Soc. Am. B* **2016**, *33*, B1.
[32] L. Mayer, T. Debuisschert, *Phys. Status Solidi A* **2016**, *213*, 2608.
[33] H. A. R. El-Ella, S. Ahmadi, A. M. Wojciechowski, A. Huck, U. L. Andersen, *Opt. Express* **2017**, *25*, 14809.
[34] K. Jensen, V. Acosta, A. Jarmola, D. Budker, *Phys. Rev. B* **2013**, *87*, 014115.
[35] D. W. Allan, *IEEE Trans. Instrum. Meas.* **1987**, *IM-36*, 646.
[36] V. M. Acosta, E. Bauch, M. P. Ledbetter, A. Waxman, L.-S. Bouchard, D. Budker, *Phys. Rev. Lett.* **2010**, *104*, 070801.
[37] H. J. Mamin, M. H. Sherwood, M. Kim, C. T. Rettner, K. Ohno, D. D. Awschalom, D. Rugar, *Phys. Rev. Lett.* **2014**, *113*, 030803.
[38] Y. Masuyama, K. Mizuno, H. Ozawa, H. Ishiwata, Y. Hatano, T. Ohshima, T. Iwasaki, M. Hatano, *Rev. Sci. Instrum.* **2018**, *89*, 125007.
[39] G. Chatzidrosos, A. Wickenbrock, L. Bougas, N. Leefer, T. Wu, K. Jensen, Y. Dumeige, D. Budker, *Phys. Rev. Appl.* **2017**, *8*, 044019.
[40] H. B. Dang, A. C. Maloof, M. V. Romalis, *Appl. Phys. Lett.* **2010**, *97*, 151110.
[41] W. C. Griffith, S. Knappe, J. Kitching, *Opt. Express* **2010**, *18*, 27167.
[42] V. K. Shah, R. T. Wakai, *Phys. Med. Biol.* **2013**, *58*, 8153.